Graphical Abstract

Advancing the Prediction of 3D Printability for Polymer Nanocomposites

Burcu Ozdemir, Miguel Hernández-del-Valle, Maggie Gaunt, Christina Schenk, Lucía Echevarría-Pastrana, Juan P. Fernandez-Blazquez, De-Yi Wang, Maciej Haranczyk

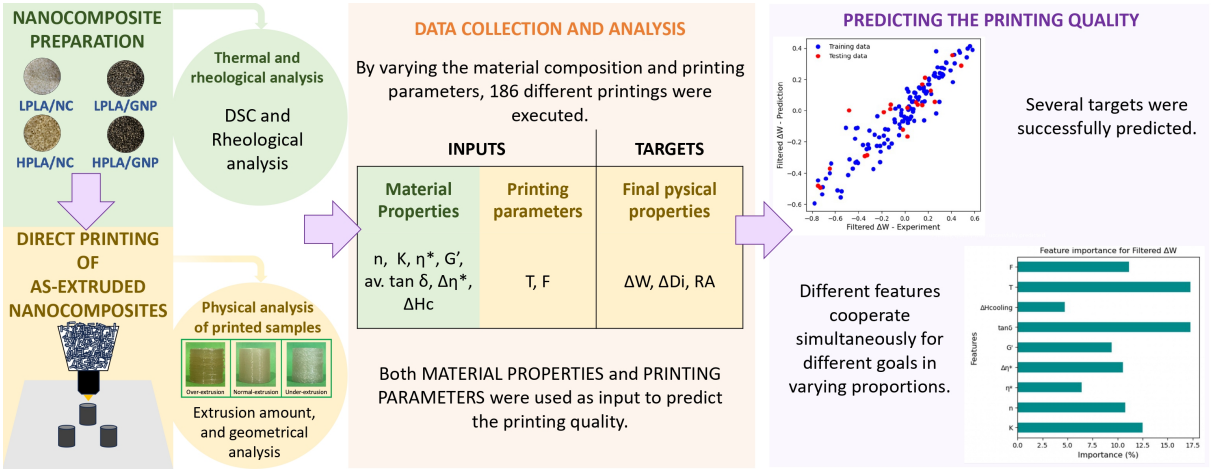

Highlights

Advancing the Prediction of 3D Printability for Polymer Nanocomposites

Burcu Ozdemir, Miguel Hernández-del-Valle, Maggie Gaunt, Christina Schenk, Lucía Echevarría-Pastrana, Juan P. Fernandez-Blazquez, De-Yi Wang, Maciej Haranczyk

- The flow index identified as the key predictor of printability.
- The flow consistency index and damping factor were identified as key predictors of extrusion.
- The flow consistency index has the most significant impact on diameter variation.
- No single property or parameter solely affects the print quality.
- Better models are needed to accurately predict surface roughness (RA).

Advancing the Prediction of 3D Printability for Polymer Nanocomposites

Burcu Ozdemir[a,b], Miguel Hernández-del-Valle[a,c], Maggie Gaunt[a,d], Christina Schenk[a], Lucía Echevarría-Pastrana[a], Juan P. Fernandez-Blazquez[a], De-Yi Wang[a], Maciej Haranczyk[a,*]

[a] *IMDEA Materials Institute, C/Eric Kandel, 2, Getafe, 28906, Madrid, Spain*
[b] *Universidad Politécnica de Madrid, 28040, Madrid, Spain*
[c] *Universidad Carlos III de Madrid, Leganes, 28911, Madrid, Spain*
[d] *Michigan State University, East Lansing, 48824, MI, USA*

Abstract

The development of new thermoplastic-based nanocomposites for, as well as using, 3D printing requires extensive experimental testing. One typically goes through many failed, or otherwise sub-optimal, iterations before finding acceptable solutions (e.g. compositions, 3D printing parameters). It is desirable to reduce the number of such iterations as well as exclude failed experiments that often require laborious disassembly and cleaning of the 3D printer. This issue could be addressed if we could understand, and ultimately predict ahead of experiments, if a given material can be 3D printed successfully. Herein, we report on our investigations into forecasting the printing and resultant properties of polymer nanocomposites while encompassing both material properties and printing parameters. To do so, nanocomposites of two different commercially available bio-based PLAs with varying concentrations of nanoclay (NC) and graphene nanoplatelets (GNP) were prepared. The thermal and rheological properties of the nanocomposites were analyzed. These materials were printed at varying temperature and flow using a pellet printer. Each time, three identical cylindrical-shaped samples were printed, and to assess the printing quality, the variation in weight and geometrical factors were determined. The interactions between material properties and printing parameters are complex but can be captured effectively by a machine learning model. Specifically, we demonstrate such a

*Corresponding author
Email address: maciej.haranczyk@imdea.org (Maciej Haranczyk)

predictive model to forecast print quality utilizing a Random Forest algorithm.

Keywords: Pellet 3D printer, Thermoplastics, Nanocomposites, Rheology, Printability, Machine Learning

1. Introduction

Thermoplastic polymer nanocomposites (PNCs) play a pivotal role across industries, embodying versatility and multifunctionality through the synergistic combination of different nanomaterials and polymers [1, 2]. Considering the increasing prevalence of 3D printing in industrial settings, there is a strong need for the development of multifunctional PNCs that are compatible with 3D printing technologies. Achieving this requires not only material design but also thorough optimization of printing settings to assure material printability and achieve the specified attributes and printing quality [3]. However, this process requires balancing multiple aspects and managing their interconnections in terms of process optimization and material design. The 3D printing process involves various factors (for example, build orientation, build sequence, slice height, printing speed, flow rate, nozzle size, layer thickness, extrusion temperature, and bed temperature) that significantly influence the ultimate quality and final properties of the printed part [4–6]. In addition to the process parameters, material properties such as thermal, mechanical, and rheological properties have a substantial impact on printability and overall performance. For example, a non-Newtonian behavior characterized by significant shear thinning has been identified as crucial for successful printing, as it ensures stable extrusion and sufficient melt strength in a semi-solid state, while extreme viscoelastic properties have been shown to prevent printing [7–9]. Furthermore, the rheological property flow index (n) has proven useful in adjusting the printing speed to achieve a consistent volumetric flow rate [10]. Moreover, minimized melting enthalpy or specific volume change has been shown to prevent geometrical instability, such as warpage, while printing polymer-based materials [11]. Considering the impact of process factors and material properties on 3D printing and final product quality, printing process optimization of PNCs requires a significant amount of trial-and-error, which results in a significant amount of material and time

waste, rendering traditional experimental methods costly. As a result, it is crucial to predict if the newly designed PNCs can be 3D printed successfully while capturing the intricate relationship between material properties and printability.

Data-driven methods have shown to be effective in optimizing process parameters and predicting final properties of 3D printed polymer-based materials [12]. Deneault et al. [13] demonstrated the possibility of application of Bayesian optimization to optimize printing parameters autonomously. Li et al. [14] showed that ensemble learning algorithms can accurately forecast the surface roughness of 3D-printed components in real-time through monitoring process parameters, and surface roughness measurements. Zhang et al. [15] used data-driven predictive modeling approach to predict the tensile strength of the co-operative printed PLA samples by considering the effect of incline angle, the overlapping length, and the number of shells on the tensile strength. Sharma et al. [16] build a model to predict the dimensional variation of 3D printed PLA and ABS specimens with different geometries using decision tree machine learning algorithm according to the effect of various printing parameters like wall thickness, infill density, build plate temperature, print speed, layer thickness, extrusion temperature.

Although these studies show the efficacy of data-driven methods in optimizing 3D-printing process parameters and predicting the properties of polymer-based materials, they often ignore material properties in the prediction algorithms and their optimization processes tailored for specific types of materials. To the best authors' knowledge, there is currently no research on PNCs that encompasses both material properties and process parameters to forecast their printing and final properties. However, in the field of food science, Ma et al. [17] conducted a noteworthy study in which they developed a predictive model to estimate the extrudability and geometry of food materials using the rheological properties of the materials and printing parameters as input parameters. By these means, they achieved relatively good machine learning predictions regarding the quality of the printed samples. The work effectively demonstrates the potential of machine learning models to capture the complex relationships specifically between material properties and their printability.

This study aims to develop a predictive model to forecast the printability and printing quality of thermoplastics and their nanocomposites by utilizing material properties as input. The model uses a variety of material attributes as input, including flow behavior, viscoelastic properties, and thermal properties, as well as printing parameters, to explore how the rheological and thermal properties of the material, along with printing factors, affect the final properties. To do so, a total of twelve binary nanocomposites were produced using two different bio-based PLAs, a commercial-grade nanoclay (NC), and graphene nanoplatelets (GNP) with a twin screw extruder (TSE). The thermal and rheological properties of the as-extruded materials, and pristine PLAs were investigated using Differential Scanning Calorimetry (DSC) and rheological (steady-state and oscillatory) analysis. The results of these analyses were used as input in the predictive model. Later, binary PNCs and pristine PLAs were printed using a commercial pellet printer by varying the temperature and flow rate, resulting in 186 independent printings. The printability and printing quality were assessed by measuring three physical properties: the weight fluctuation of the printed cylinders to determine whether they were over- or under-extruded, and the interior diameter and surface uniformity of the cylinders using digital image analysis. The relationship between material characteristics (thermal and rheological), printing parameters (temperature and flow), and printing quality first was analyzed by checking correlations via the Pearson correlation coefficient. Subsequently, a random forest algorithm was used to predict printing quality. The feature importance analysis was used to identify which material properties had the greatest impact on printing quality.

2. Materials and methods

2.1. Materials

Two commercially available bio-based PLA grades were supplied from NatureWorks LLC, USA: Ingeo 4043D and Ingeo 3251D, with melt flow index (MFI, at 210°C with 2.16 kg) of 6 g/10min and 80 g/10min, respectively. The samples, both having densities of 1.24 g/cc, were designated as HPLA and LPLA, respectively, for high and low molecular

weight. The commercial NC (Cloisite 30B, ∼6-13 μm) was provided by Southern Clay Products, Texas, USA, and commercial GNP (xGnP M-5, ∼5 μm) were purchased from Sigma-Aldrich Chemical Co. Both nanoparticles were used without any surface treatment.

2.2. Nanocomposite preparation

Masterbatches of 10 wt% of HPLA/NC, HPLA/GNP, LPLA/NC, and LPLA/GNP were prepared using a counter-rotation twin-screw extruder with L/D ratio of 40:20. Then, the master batches were diluted with pure PLA to make nanocomposites with composition of 0.5, 1, and 3 wt.%. HPLA and LPLA nanocomposites were processed at 180°C and 170°C, respectively, while keeping the speed at 80 rpm in both cases. All of the materials were dried overnight at 80°C before processing.

2.3. Characterisation of as-extruded nanocomposites

2.3.1. Differential scanning calorimetry (DSC) and scanning electronic microscopy (SEM) analysis

The crystallization behavior and transition temperatures of neat PLAs and as-extruded nanocomposites were analyzed using a DSC (TA Instruments Q200) in a heat-cool-heat cycle at a rate of 10°C/min under nitrogen atmosphere. The crystallization degree (X_c) was calculated during heating and cooling cycles using equations (1), and (2), respectively.

$$X_c^{heating} = \frac{(\Delta H_m - \Delta H_{cc}) \cdot 100}{\omega_{PLA} \Delta H_m^0} \tag{1}$$

$$X_c^{cooling} = \frac{\Delta H_c \cdot 100}{\omega_{PLA} \Delta H_m^0} \tag{2}$$

where ΔH_m, ΔH_{cc}, and ΔH_c are heat enthalpies of melting, cold crystallization, and crystallization, respectively. ω_{PLA} is the weight fraction of PLA in the nanocomposite, and ΔH_m^0 is the heat of fusion for 100% crystalline PLA, which is 93.6 J/g [18].

The morphology of the gold-coated samples was investigated by a SEM (ZEISS EVO MA 15) at an accelerating voltage of 5 kV.

2.3.2. Steady-state and oscillatory rheological analysis

The rheological measurements were carried out with an MCR-702e rotational rheometer (Anton Paar, Austria) equipped with a 25 mm diameter parallel-plate. To evaluate the steady flow behavior of the materials, steady-state shear tests were performed at 180°C within a shear rate range of 0.05-100s^{-1}, with a measuring gap of 0.5 mm. Later, the flow parameters were determined by fitting the experimentally obtained viscosity data at low shear rates ($\dot{\gamma} < 10s^{-1}$) to the power-law fluid model (Eq. 3)[19].

$$\eta = K\dot{\gamma}^{n-1} \tag{3}$$

where η is the viscosity (Pa.s), K is the flow consistency coefficient, n is the flow index, and $\dot{\gamma}$ is the shear rate (s^{-1}).

To assess thermal stability and viscoelastic behavior of the nanocomposites, oscillatory time sweep tests were conducted at varying temperatures matching the printing temperatures, each lasting 20 minutes. The tests were conducted within the linear viscoelastic region (LVR), maintaining a fixed strain amplitude and angular frequency of 1/s with a 1 mm measuring gap. The change of complex viscosity in each test was calculated using the following equation:

$$\%\Delta\eta^* = \frac{\eta_f^* - \eta_i^*}{\eta_i^*} x100 \tag{4}$$

where η_i^* is the initial complex viscosity, η_f^* is the final complex vicosity after 20 minutes, and $\%\Delta\eta^*$ is the percent change in complex viscosity during a 20 minutes of time sweep test.

2.4. Printing

As-extruded HPLA/NC, HPLA/GNP, LPLA/NC, and LPLA/GNP pellets, as well as the pristine HPLA and LPLA, were directly fed into the Direct3D F30 pellet printer after drying overnight at 80°C. Pellet printing was specifically chosen because of its suitability for automated material design [20]. To investigate the effect of nozzle temperature and extrusion flow on the printability and final properties of samples, three cylindrical

specimen samples (D_e:20mm, D_i:15.2mm, h:20mm) of each composition were printed at varying temperatures and extrusion flows. Table 1 shows the printing parameters. The printing speed is represented as a percentage relative to the standard speed chosen by the slicer. The extrusion flow is a multiplier expressed as a percentage. It is used to convert the millimeters determined by the slicer for a filament to be extruded into revolutions of the internal screw of the pellet printer.

Table 1: Printing Parameters

Parameter (units)	Value
Nozzle temperature (°C)	180 - 220
Bed temperature (°C)	50
Extrusion flow (%)	1500 - 3000
Layer height (mm)	0.2
Layer Width (mm)	0.6
Printing speed (%)	50
Nozzle size (mm)	0.8

2.5. Determination of printing quality

The printing parameters and material properties have a notable influence on the physical and geometrical characteristics of the printed samples, such as extrusion stability, layer periodicity, and the uniformity of printed cylindrical specimens. Extrusion stability, in other terms, over- or under-extrusion (ΔW) was assessed by measuring the weights of the three samples after each printing, which was averaged and reported as the printed weight (W_{printed}). Knowing the theoretical density of the nanocomposite contents and volume of the cylinders, the theoretical weight ($W_{\text{theoretical}}$) of the samples was calculated for each composition at 100% infill rate. Finally, ΔW was calculated using the following formula:

$$\Delta W = \frac{W_{\text{printed}}}{W_{\text{theoretical}}} - 1 \tag{5}$$

To evaluate the geometrical quality of the samples, the roughness average (RA) and internal diameter (D_i) of the printed samples were determined using image processing techniques. This work utilizes the image processing techniques presented in our previous

study [20]. RA, which is a commonly used parameter to assess surface quality [21], quantifies the average variation of the surface profile from its primary profile or center line over a specified evaluation length. It is defined as follows:

$$RA = \frac{1}{L} \int_0^L |x(y)|\, dy \tag{6}$$

where L denotes the designated length of interest for roughness evaluation, the function $x(y)$ is the surface profile's vertical height deviation from a primary reference line at a precise position y within this specified length. The capability of our system to enable a resolution of one pixel is roughly 0.1mm. Considering that the layer height was fixed at 0.2 mm, which corresponds to 2 pixels, the resolution of the utilized system is not sufficient for examining intralayer quality.The primary profiles of the cylinders were determined through linear regression, using the points corresponding to various contours on both sides of the printed cylinder sample.

The main interest in terms of the geometrical analysis of this study lies in identifying the irregularities in the printed samples. The method for determining the inner diameter of the samples through image analysis relies on assessing the cylinder's adherence height to the cone. This method allows for the identification of the contours on both the left and right sides of the cylinder, which are situated between the top and bottom corners. After the inner diameter is calculated, the deviation of the inner diameter from the expected diameter (ΔD_i) is calculated with an equation similar to Equation 5.

2.6. Descriptors, Dataset, and Model

The study aims to predict the printability and printing quality of the thermoplastics and their nanocomposites while innovatively using the material properties as input for the predictive model. Table 2 summarizes the input parameters used for the prediction model. The flow index (n) and flow consistency index (K), determined by steady-state rheological analysis, were utilized as flow indicator inputs. The initial complex viscosity (η^*), initial storage modulus (G'), and average loss factor (av. $\tan\delta$) determined by time sweep experiments were utilized as viscoelastic property inputs. During the initial trial-and-error-experiments, it was noticed that some materials undergo thermal degradation,

which affects the printing process and final quality. As a result, the change in complex viscosity (% $\Delta\eta^*$) determined by time sweep tests is utilized as input since it indicates thermal stability. Candal et. al. [11] showed that a minimized melting enthalpy or specific volume change are favourable to prevent warpage or geometrical instability. Inspired by that study, the crystallization enthalpy (ΔH_c) determined by DSC measurements was utilized as input. Finally, printing parameters namely, extruder temperature (T), and extrusion flow (F) were also utilized as input. The over-/under-extrusion and geometrical features of the printed samples were determined and these values were introduced as output.

Table 2: Description of input parameters for the prediction model.

Parameter	**Units**	**Description**
n	dimensionless	flow index
K	Pa·s^n	flow consistency index
η^*	Pa·s	initial complex viscosity
G'	Pa	initial storage modulus
av. $\tan\delta$	dimensionless	average loss factor
$\Delta\eta^*$	dimensionless	change in complex viscosity in 20 min
ΔH_c	J/g	crystallization enthalpy
T	°C	printing temperature
F	%	extrusion flow

The random forest (RF) machine learning algorithm, which is based on an ensemble of multiple decision trees [22] was utilized (1) to predict the extrusion and geometrical features and (2) to determine the importance of the material features for the printability and final properties. The RandomForestRegressor class from the sklearn.ensemble package in Python was employed for this purpose [23]. Initially, the dataset was randomly split into a training set (85%) and a test set (15%). The hyperparameters of the prediction model are number of trees in the forest (n_estimators), the maximum depth of the tree (max_depth), the minimum number of samples required to split an internal node (min_samples_split), the minimum number of samples required to be at a leaf node (min_samples_leaf), and the number of features to consider when looking for the best split (max_features) [24, 25].

Grid search of these hyperparameters was performed, utilizing cross-validation with five folds to ensure robust performance evaluation. Table 3 shows the hyperparameters of each model. To assess and validate the RF prediction model, the squared correlation coefficient (R^2) and the mean absolute error (MAE) were calculated using the functions from Scikit-learn in Python: r2_score and mean_absolute_error, respectively [23].

Table 3: Hyperparameters for different target parameters.

Target	**n_est**	**max_feat**	**max_depth**	**min_leaf**	**min_split**	**rand_state**
ΔW	10	8	10	2	2	201
Filtered ΔW	1500	8	10	2	2	201
Filtered ΔDi	100	5	10	2	2	201
Filtered RA (mm)	500	3	7	2	7	201

3. Results and Discussion

3.1. Characterisation of PNCs

3.1.1. Morphological analysis of PNCs

To assess the extent of dispersion of NC and GNP in PLAs, SEM analysis was utilized. Figure 1 presents the SEM micrographs of the as-extruded pure PLAs and PNCs. The fracture surfaces of the neat PLAs looks smooth which is specific to brittle polymers. The SEM micrographs of PLA/GNP nanocomposites depict non-functionalized GNPs dispersed in stacked layers, partly exfoliated, with a nanoplatelet morphology characterized by a micron-scale length 0.5–2 µm and a nanoscale thickness. Similarly, layers with micron-scale lengths and nanoscale thicknesses, were observed in PLA/NC samples, while the NC exhibited better intercalation compared to GNP. This enhanced intercalation of NC is attributed to interactions between the hydroxyl groups of the organo-modified NC (Cloisite 30B) and the carboxyl groups of PLA which promotes clay dispersion within PLA matrices [26].

3.1.2. Steady-state shear flow of PNCs

Figure 2a and b depict the variation of viscosity with steady shear rate for PLAs with NC and GNP, respectively. The viscosity of pristine HPLA is more than an order

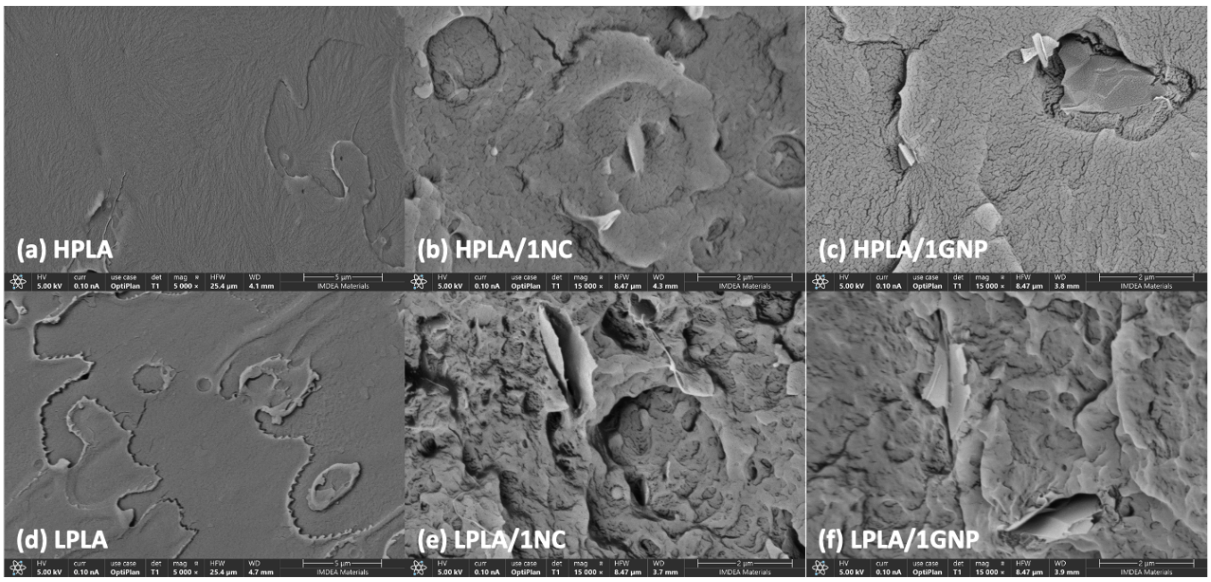

Figure 1: SEM micrographs of extruded nanocomposites: (a), (d) HPLA and LPLA, respectively, at 5K magnification; (b), (e) HPLA/1NC and LPLA/1NC; (c), (f) HPLA/1GNP and LPLA/1GNP at 15K magnification.

of magnitude higher than that of pristine LPLA in the low-shear rate region, consistent with the higher molecular weight of HPLA, compared to that of LPLA. The viscosity curves of all of the nanocomposites appear to fall under their pristine counterparts. In the case of nanocomposites with GNP (Fig. 2b), the reduction in the viscosity curves is more pronounced compared to their counterparts containing NC (Fig. 2 a). Although the reductions in the viscosity curves of HPLA/NC and HPLA/GNP are correlated with the additive content, the changes in the viscosity values of the LPLA/NC and LPLA/GNP samples are not correlated with additive content.

The viscosity-shear rate curves not only demonstrate the flow behaviour but also offer insights into the dispersion state of the nanofiller within the polymer matrix as well as their interaction. When a good nanofiller dispersion is achieved the viscosity of the material is increased, and above the percolation threshold concentration, significant shear-thinning is observed [7, 8]. Although SEM images presented in Figure 1 revealed a good dispersion of NC and GNP, in Figure 2 nanocomposites exhibited lower viscosity values. Such reduction in the viscosities of the nanocomposites suggests the involvement of potential factors such

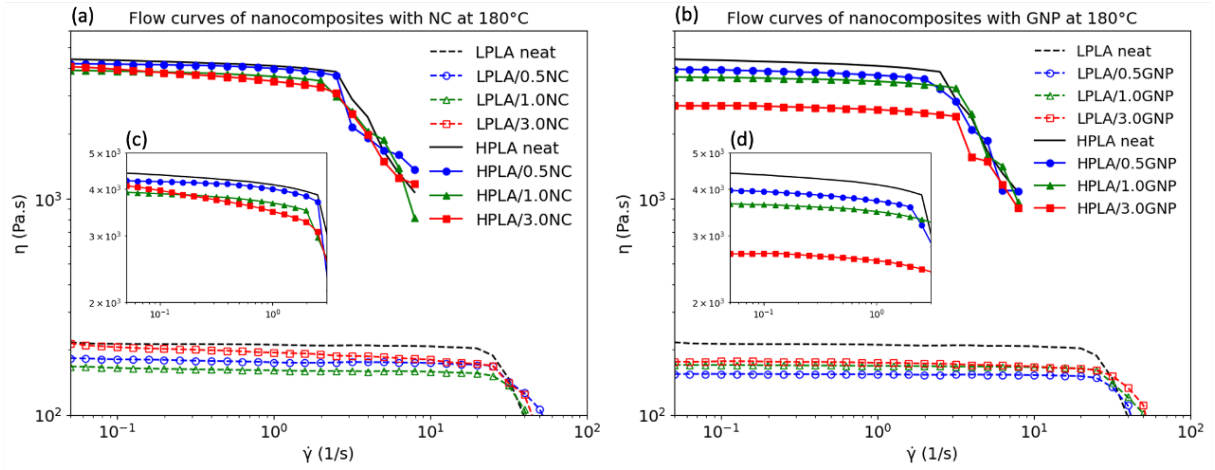

Figure 2: Change of viscosity with steady shear rate for: a. HPLA/NC and LPLA/NC nanocomposites, b. HPLA/GNP and LPLA/GNP nanocomposites at 180°C. Close-up view of c. HPLA/NC nanocomposites and d. HPLA/GNP nanocomposites.

as, the possibility of thermal degradation triggered by high-temperature treatments, and the plasticizing effects of the nanofillers. In the case of nanocomposites with NC, prior studies [26, 27] have indicated that although the introduction of organically modified NC enhances the mechanical and barrier properties of PLA, during high-temperature treatment, the thermal degradation of PLA intensifies significantly when clay is incorporated. The surfactants present in organo-modified clay seem to exacerbate the thermal degradation of the PLA, as their thermal decomposition byproducts act as catalyst agents. This degradation leads to a decrease in molecular weight and, consequently, a reduction in viscosity. On the other hand, in case of nanocomposites with GNP, studies have reported a plasticizing effect of GNP on PLA's rheological properties due to the presence of hydrodynamic slip effects and weak interfacial interactions between GNP and the polymer. When shear is applied, the nanoplatelets of GNP align in the direction of shear, facilitating a lubricating flow and, thus, promoting plasticization of PLA. It was further noted that this behavior was exclusively observable under steady shear conditions, and no similar behavior was observed under oscillatory shear [7, 8].

Table 4 presents the flow parameters calculated by fitting the experimental data to the power-law fluid model (Eq. 3). Here, flow consistency coefficient K provides insight

Table 4: Calculated flow consistency coefficient (K) and flow index (n) of the neat polymers and nanocomposites

Sample Name	**K**	**n**	**Sample Name**	**K**	**n**
LPLA neat	211	0.99			
LPLA/0.5NC	176	0.99	LPLA/0.5GNP	154	1.00
LPLA/1.0NC	161	0.99	LPLA/1.0GNP	168	1.00
LPLA/3.0NC	193	0.97	LPLA/3.0GNP	170	0.97
HPLA neat	4,075	0.97			
HPLA/0.5NC	3,959	0.97	HPLA/0.5GNP	3,656	0.97
HPLA/1.0NC	3,581	0.96	HPLA/1.0GNP	3,462	0.98
HPLA/3.0NC	3,398	0.93	HPLA/3.0GNP	2,572	0.98

into the average viscosity of the material. Accordingly, HPLA has a K indices around 4000 while this value is around 200 for LPLA. The K indices of all of the nanocomposites also reduced compared to their pristine counterparts while the reduction is more for GNP containing nanocomposites. The n index in Table 4 gives insight about the shear-thinning behavior. A slope with n value of 1 represents perfect Newtonian behaviour, while reduction in n index is correlated with shear thinning behaviour. As a result, n index is a good indicator of the behaviour of the viscosity curve. The pristine PLAs, HPLA and LPLA, exhibit Newtonian plateaus with narrow ($\dot{\gamma} < 2/s$) and wide plateau ($\dot{\gamma} < 20/s$) regions, respectively. There is not a significant difference in the flow indices of HPLA nanocomposites, except the HPLA/3NC which has the lowest n index. Similary, in case of LPLA nanocomposites the difference is not noticable with n index values closer to 1 while LPLA/3NC and LPLA/3GNP has lower n index compared to other LPLA nanocomposites. The K and n indices effectively characterize the material's flow behavior; and, they have been proven to be reliable inputs for predicting the material's printing behavior [17]. Accordingly, the values reported in Table 4 were used as input values for the predictive model.

3.1.3. Viscoelastic properties and thermal stability of the PNCs

The viscoelastic properties of thermoplastics are influenced by both time and temperature of measurements. Similarly, 3D printing is a time- and temperature-dependent

process, which in turn affects the printability of the material under specific printing conditions. Moreover, PNCs can experience thermal degradation at high temperatures, which can negatively impact their flow during the printing process. As a result, this work aims to explore how material viscoelastic properties, including complex viscosity, storage modulus, and damping factor, as well as thermal stability, affect printability of material and prediction of printing quality. Based on these factors, rheological time sweep tests were utilized to collect information on the as-extruded PNCs and pristine polymers. Time sweep tests of 20 min were conducted at corresponding printing temperatures for each material. The storage modulus and complex viscosity of the samples were collected from the second minute of the time-sweep tests. Moreover, the loss factors of the samples calculated from the 20 min time-sweep test were collected and utilized after averaging. The results of these measurements, which are not presented here, were utilized as input for the machine learning algorithm.

To understand the thermal stability of the samples, the percent change in the complex viscosity (% $\Delta\eta^*$) in 20 min of time sweep test was calculated. The box plots in Figure 3 illustrate the distribution of % $\Delta\eta^*$ for PNCs versus compositions. Here, each box displays the distribution of % $\Delta\eta^*$ values for a particular composition measured at various temperatures. In each box, five data points are shown for HPLA and its nanocomposites within the temperature range of 180 to 220°C, while four data points are presented for LPLA and its nanocomposites within the range of 180 to 210°C. Complex viscosity of the pristine HPLA decreased between 0 to 20% during time sweep experiments at various temperatures, whereas complex viscosity of pristine LPLA decreased between 10 to 30% at various temperatures. The reduction in complex viscosity of pristine polymers during the time sweep tests is likely attributed to the thermal degradation of PLA. High-temperature processing is known to induce degradation in PLA, stemming from reactions such as hydrolysis, inter-chain transesterification, and intramolecular transesterification. As these reactions lead to a reduction in molecular weight, it's noteworthy that during time sweep tests, which involve a form of thermal treatment, there is a corresponding decrease in complex viscosity [28, 29]. Overall, it appears that pristine HPLA exhibits

better thermal stability compared to pristine LPLA. The presence of active sites on the chain ends of PLA causes depolymerization by back-biting (chain end scission or intramolecular transesterification) during high-temperature treatment [30]. Since pristine LPLA has more chain ends due to its lower molecular weight, its lower thermal stability could be attributed to the higher likelihood of depolymerization by back-biting during high-temperature treatment.

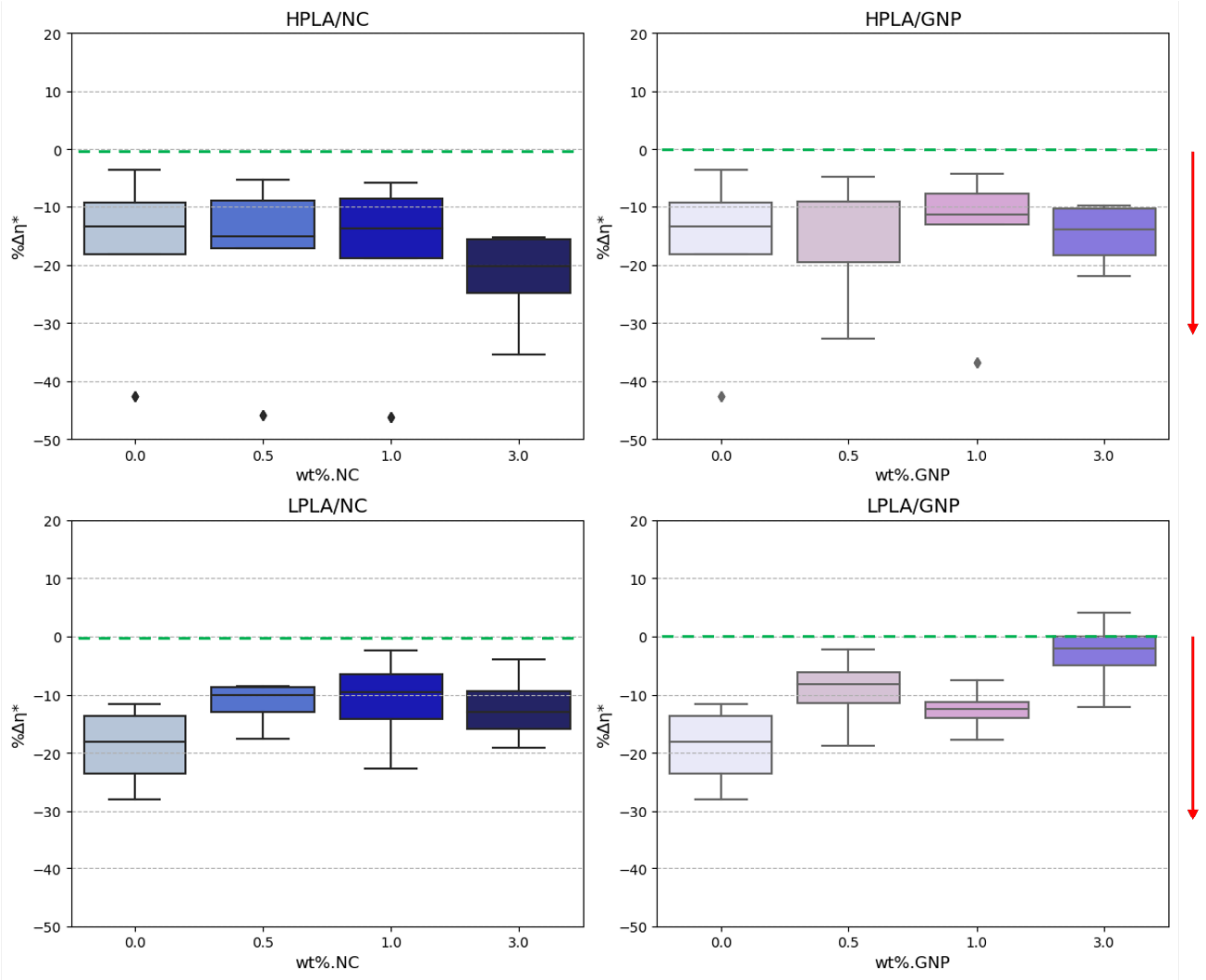

Figure 3: Change of complex viscosity (%) at different temperatures for: a. HPLA/NC, b. HPLA/GNP, c. LPLA/NC, and d. LPLA/GNP nanocomposites. Negative change in the viscosity indicated by red arrow that implies the complex viscosity decreased during the time sweep test.

All of the nanocomposites also exhibited negative % $\Delta\eta^*$, indicating thermal degradation, which was found to be strongly affected by the type of PLA, additive, and composi-

tion. Introducing 0.5 or 1 wt.% of NC into HPLA (Figure 3.a) did not noticeably alter % $\Delta\eta^*$ until reaching 3 wt.%, at which point the viscosity reduction became severe, ranging from -15 to -35 wt.%. Adding GNP to HPLA (Figure 3.b) changed the % $\Delta\eta^*$ distribution to a more stable variant, reducing the outliers seen in HPLA/NC to a lesser extent in HPLA/GNP. In contrast, the addition of NC and GNP into LPLA (Figure 3.c and d) substantially mitigated the reduction in viscosity, indicating improved thermal stability, particularly with GNP. The different impact of NC on the % $\Delta\eta^*$ of HPLA and LPLA, suggests a dynamic interplay between thermal degradation and rheological enhancement influenced by the exfoliation state of NC within the different molecular weight polymer matrices. The effect of NC on thermal degradation depends greatly on its quantity and the level of dispersion within the polymer matrix. As the degree of NC dispersion increases, its impact on thermal degradation becomes more significant. [27]. Finally, it should be noted that compared to NC-containing counterparts, addition of the GNP in the structure improved the thermal stability of the nanocomposites. This enhancement is attributed to the shielding effect provided by the flake-like structure of GNPs, which effectively hinders the diffusion of volatile decomposition products within the nanocomposites [31, 32].

3.1.4. DSC analysis of PNCs

The DSC cooling and second heating thermograms of virgin PLAs and nanocomposites are illustrated in Figure 4. Figure 4a shows the cooling curves of pure HPLA and its nanocomposites without any crystallization occurring in either material. While the introduction of nanomaterials could not promote crystallization, due to the large molecular weight and high D-lactide content (4.25 mol%) of HPLA, it is reasonable to expect that HPLA will not crystallize when rapidly cooled (10°C/min). Figure 4b depicts the second heating curves of the same materials. While HPLA showed a very weak cold crystallization peak around 120°C, with the introduction of GNP and NC, the cold crystallization peaks started at earlier temperatures around 100 and 110°C, respectively. This demonstrates the nanomaterial's nucleation effect on HPLA crystallization. However, in the case of HPLA/NC samples, cold crystallization started earlier compared to HPLA/GNP samples. According to the steady-state viscosity analysis, HPLA/GNP samples have a much

lower viscosity, resulting in higher mobility. However, rheological time sweep analysis revealed higher thermal degradation in HPLA/NC samples, and a similar situation could occur during DSC. As a result of thermal degradation and lower chain length, HPLA/NC could have earlier cold crystallization due to higher chain mobility.

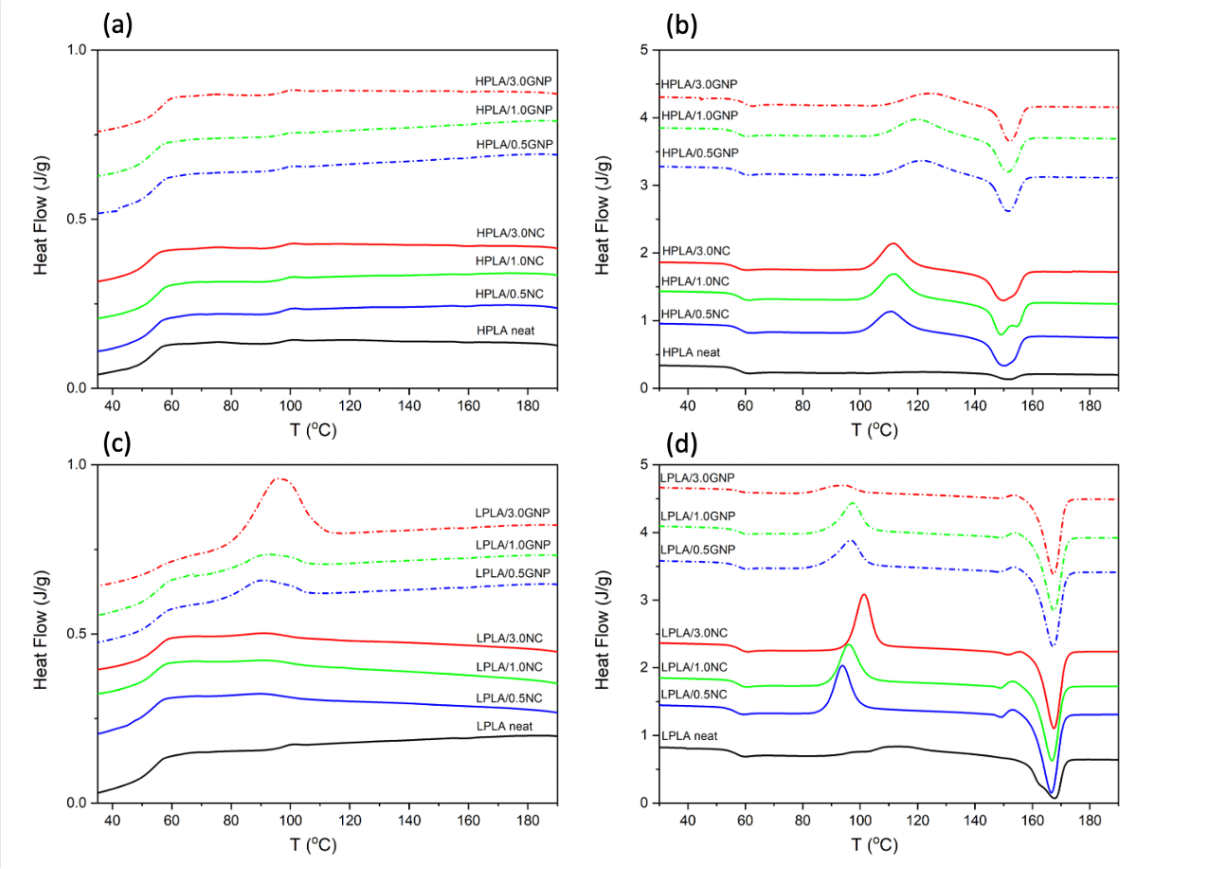

Figure 4: DSC cooling (a, c) and 2nd heating (b, d) thermograms of HPLA/NC, LPLA/NC, HPLA/GNP, and LPLA/GNP.

Figure 4c depicts the cooling curves of pure LPLA and its nanocomposites. Although having a much lower molecular weight and a lower D-lactide content (1.4 mol%), LPLA could not crystallize during cooling either due to rapid cooling. The addition of NC and GNP accelerated crystallization during cooling by acting as heteregenous nucleation points. This effect was much stronger in the LPLA/GNP samples. While the crystallisation percent of the LPLA/NC ones ranged from 4% to 6%, this range increased to 9% to 31% for the LPLA/GNP ones. This could be due to the higher mobility of the

Table 5: Transition temperatues and crystallinities of the neat PLAs, and PLA nanocomposites.

	$T_g^{cooling}$	$T_c^{cooling}$	T_g^{h2}	T_{cc2}	T_m^{h2}	$X_c^{cooling}$ (%)	$X_c^{heating}$ (%)
HPLA	54	no data	58	120	152	0	1
HPLA/0.5NC	55	no data	59	111	150	0	1
HPLA/1.0NC	56	no data	58	112	150, 155	0	1
HPLA/3.0NC	54	no data	57	111	150, 155	0	1
HPLA/0.5GNP	55	no data	58	121	151	0	1
HPLA/1.0GNP	54	no data	58	120	151	0	1
HPLA/3.0GNP	57	no data	57	124	152	0	0
LPLA	55	no data	57	113	168	0	1
LPLA/0.5NC	55	91	56	94	167	4	2
LPLA/1.0NC	54	93	58	96	167	4	1
LPLA/3.0NC	56	92	58	101	167	6	3
LPLA/0.5GNP	56	90	58	97	167	12	13
LPLA/1.0GNP	57	91	58	97	168	9	12
LPLA/3.0GNP	56	95	58	95	167	31	35

LPLA/GNP samples, which facilitated easier chain alignment and crystallization. Figure 4d shows the second heating curves of the same materials. Neat LPLA showed a cold crystallization starting around 90°C. The addition of NC initiated cold crystallization around 80°C, and this temperature increased with the NC content. This is in line with the finding that the material had higher viscosity thus less mobility in the steady-state rheological analysis with increased NC content. The cold crystallisation of the LPLA/GNP samples started around 80°C and cold crystallization peak got smaller with 3wt.% of GNP. The steady-state viscosity analysis showed that the LPLA/GNP samples have higher mobility, which causes that the mostly of the crystallization was carried out during cooling. When the LPLA and HPLA nanocomposites are compared, the heterogeneous nucleation effect of nanomaterials is more significant in the case of LPLA due to its lower molecular weight and D-lactide content, while the LPLA/GNP samples have the highest crystallinity.

3.2. Characterisation of printed samples

3.2.1. Assessment of over-/under-extrusion

The variation in the extrusion during printing is highly dependent on the printing parameters as well as material's rheological and thermal properties. Under the same printing conditions materials with different rheological properties exhibit different flow properties as well as variation in the extrusion. Similarly, possibility of thermal degradation could also prevent proper extrusion. Before going into further discussion about the extrusion, examples of over, normal, and under extruded samples are presented in Figure 5.

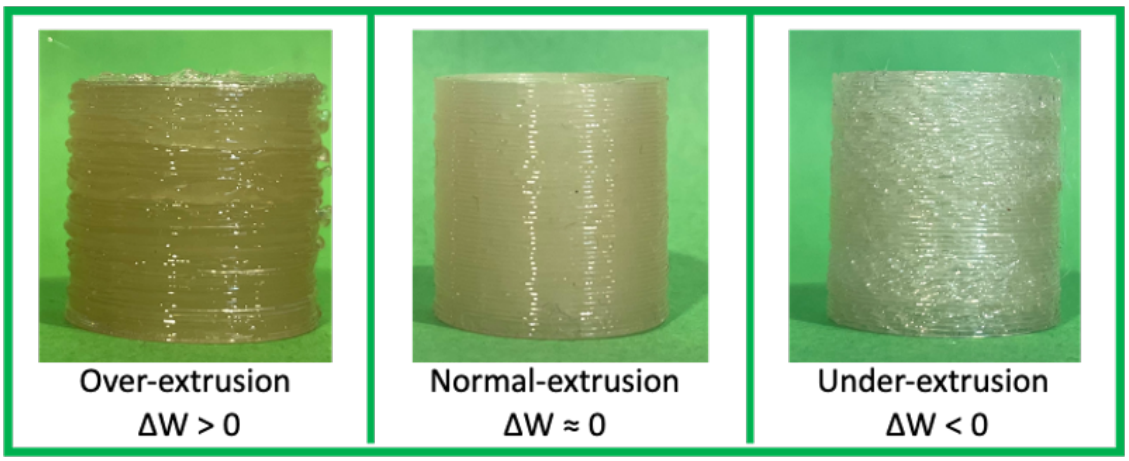

Figure 5: Examples of over, normal, and under extruded samples.

To assess the extent of under or over-extrusion, the weight of the printed samples was measured, and the variation between the measured and theoretical values (ΔW) was calculated. Figure 6 depicts the variance of ΔW with respect to composition, with each box representing the distribution of ΔW determined for several printings of a single composition under varied printing conditions. The dashed green line indicates ΔW equal to zero, where the printed sample matches the calculated weight of the design. A positive ΔW value indicates over-extrusion, where the printed sample weighs more than the calculated value of the designed sample, while a negative ΔW represents under-extrusion where the printed sample weighs less than the calculated value of the designed sample. The ΔW box of pristine HPLA is located just below the zero-line while the one that of LPLA is located just above the zero line. This indicates that while most of the pristine HPLA samples

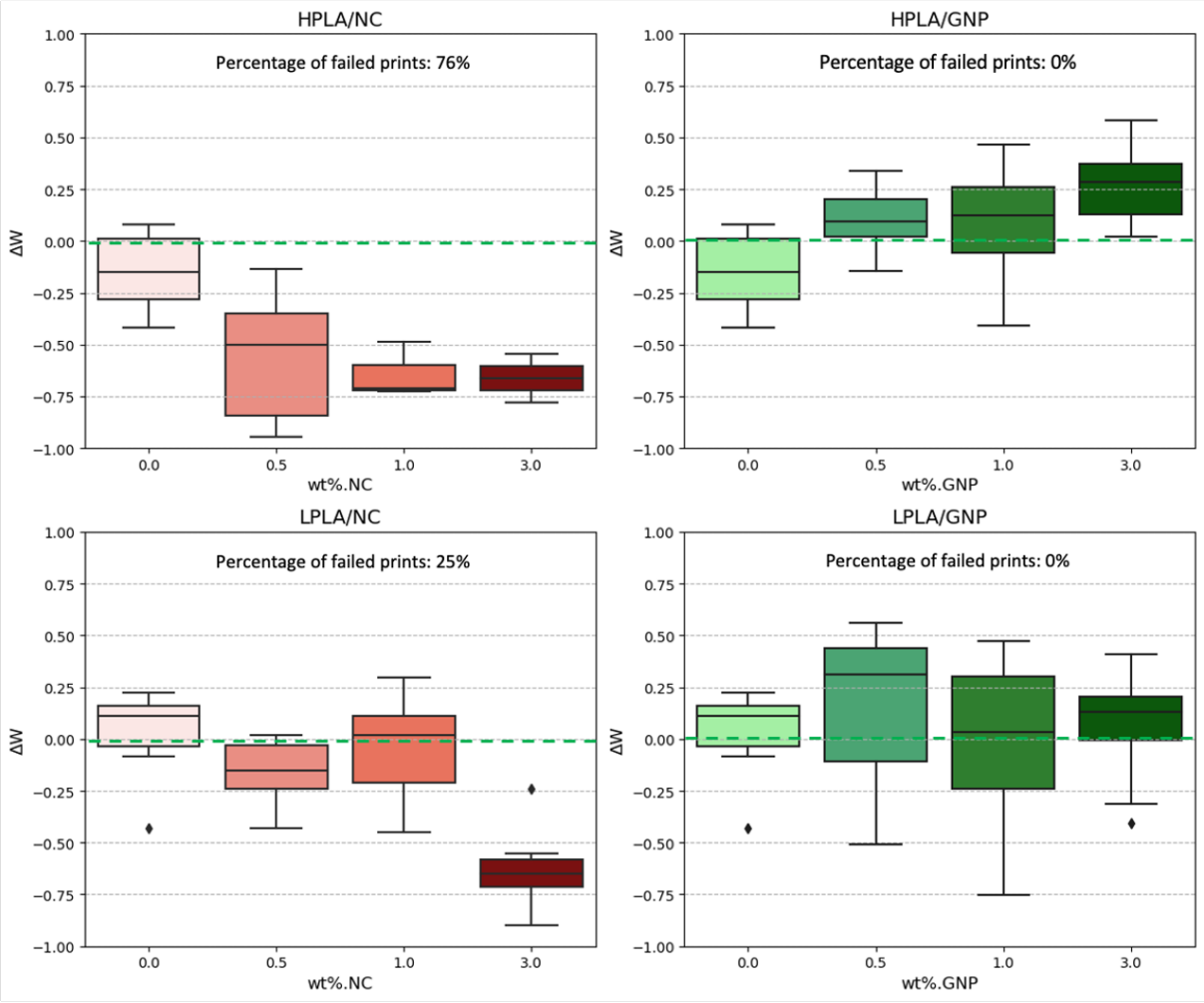

Figure 6: Weigh variation (ΔW) of the nanocomposites with respect to composition.

under-extruded, most of the LPLA samples over-extruded. Considering the higher viscosity of the HPLA compared to that of LPLA, it is expected for HPLA to exhibit more under-extrusion compared to LPLA. When NC incorporated into HPLA, ΔW boxes of the HPLA/NC nanocomposites shifted entirely below the zero line, and the position of the median and the box moved lower as the NC content increased in the composition. It is important to note that 76% of the HPLA/NC samples failed to print which includes some of the HPLA/1.0NC samples, and the majority of the HPLA/3.0NC samples. In general it could be concluded that altough, the introduction of the NC did not increase the viscosity of the nanocomposites (Fig. 2), the increase in the storage modulus and

thermal degradation (Fig. 3) could collaboratively acted and result in under-extrusion while making printing impossible after some point.

When GNP incorporated to HPLA, ΔW boxes moved almost entirely above the zero line, showing a general trend of over-extrusion in the printing of HPLA/GNP, and this over-extrusion is correlated with GNP content. It is noteworthy that all HPLA/GNP samples were successfully printed under various conditions, with varying degrees of quality. This is consistent with the reduced viscosity of HPLA/GNP nanocomposites resulted from the lubricating effect of GNPs and in addition to the better thermal stability. In case of LPLA, when NC incorporated ΔW boxes shifted to negative values. Although LPLA/NC samples have lower viscosity and better thermal stability compared to HPLA/NC and HPLA/GNP still 25% of the LPLA/NC samples failed to print. When GNP introduced to the LPLA samples, the variation of the ΔW boxes increased but the majority of the samples exhibited over-extrusion due to a lubricating effect of GNP.

3.2.2. Assessment of geometrical features of PNCs

In order to evaluate the geometrical quality of the samples, the roughness average (RA) and internal diameter (D_i) of the printed samples were determined using image processing techniques as reported in our previous work [20]. The geometrical analysis includes samples with ΔW greater than or equal to -0.8, while samples with ΔW between -0.8 and -1 could not be analyzed. Figure 7 shows the variation in internal diameter determined using the same approach as equation 5, and 0 indicates the exact diameter indicated in the CAD design was achieved. All materials exhibited a diameter reduction ranging from 2-15%. HPLA/NC samples showed less variation in D_i possibly due to higher viscosity of the materials. However, it is important to note that most of the HPLA/NC samples failed to be printed and there is significantly less data for these samples resulting in narrow distribution in the box plot. In the instance of HPLA/GNP, which had less viscosity and more over-extrusion compared to HPLA/NC, D_i significantly decreased due to over-extrusion of the material and the trend of ΔD_i is negatively correlated with the ΔW trend. In case of LPLA/NC that had very low viscosity and slight-underextrusion, the D_i found to be closer to the expected value with a variation in the samples due to

the under extruded samples. In case of LPLA/GNP, having the lowest viscosity and most significant over-extrusion, all of the samples had decreased D_i due to the over-extrusion during printing. These results indicates a direct correlation between viscosity of the samples and ΔD_i and a negative correlation between ΔD_i and ΔW.

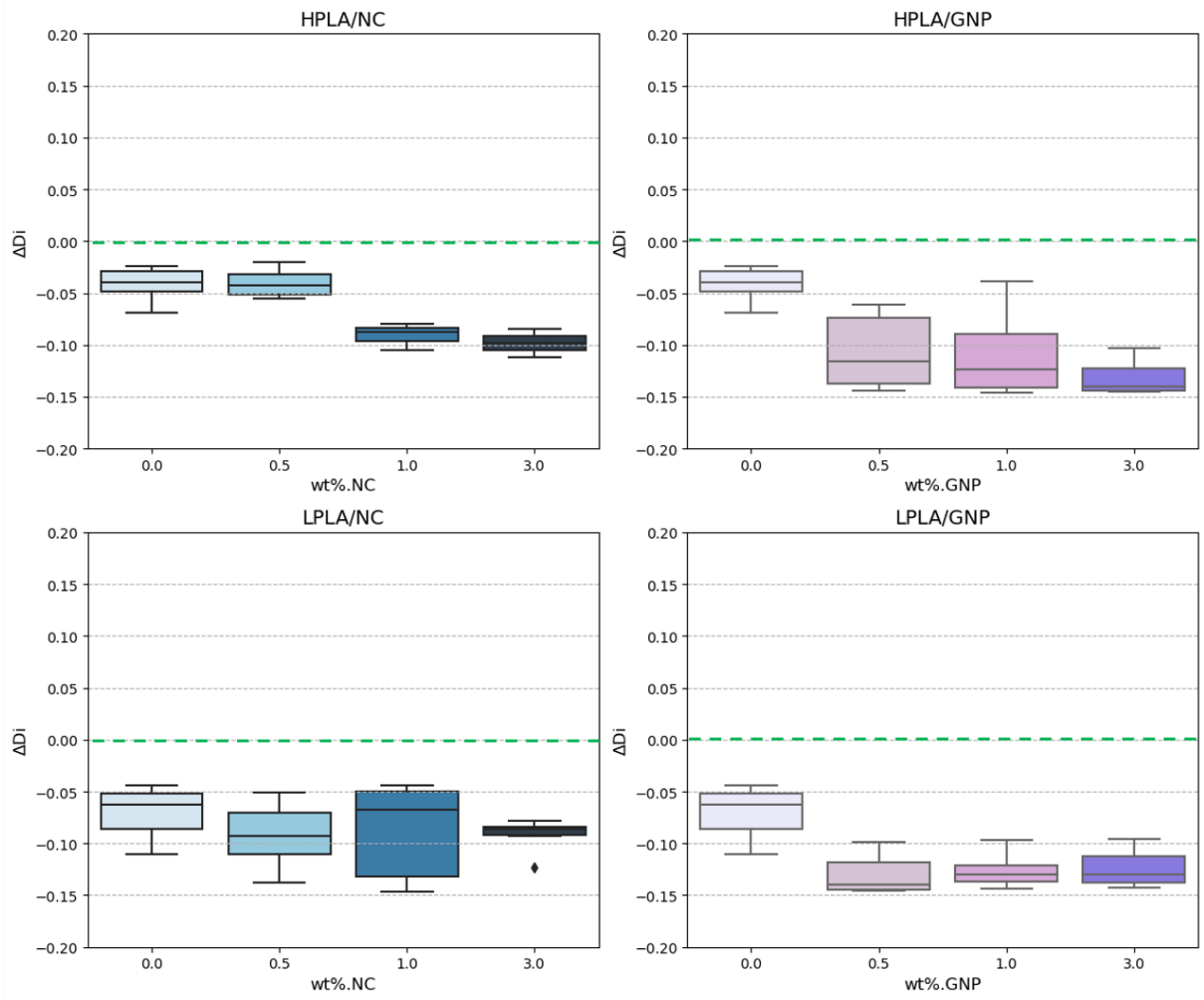

Figure 7: Diameter variation (ΔD_i) of the nanocomposites with respect to composition.

Figure 8 depicts the RA in mm versus composition, with 0 being a perfectly smooth surface. Upon comparing virgin LPLA with HPLA, it is evident that LPLA exhibits a higher surface roughness, likely attributed to its over-extrusion during printing resulting from its lower viscosity compared to that of HPLA. However, when comparing HPLA/NC, which displayed severe under-extrusion, to HPLA/GNP, which exhibited over-extrusion,

RA is significantly higher in HPLA/NC samples, most likely due to under-extrusion, which resulted in unfilled structural gaps. However, when LPLA/GNP displayed significant over-extrusion, the RA increased, most likely because to the uneven layers produced. These trends suggest that, while low viscosity or over-extrusion during printing can raise the roughness average by resulting in larger and irregular layers, high viscosity or under-extrusion can also increase the roughness average by resulting in unfilled layers during printing. As a result, it is hard to deduce a direct correlation between RA with viscosity, and ΔW.

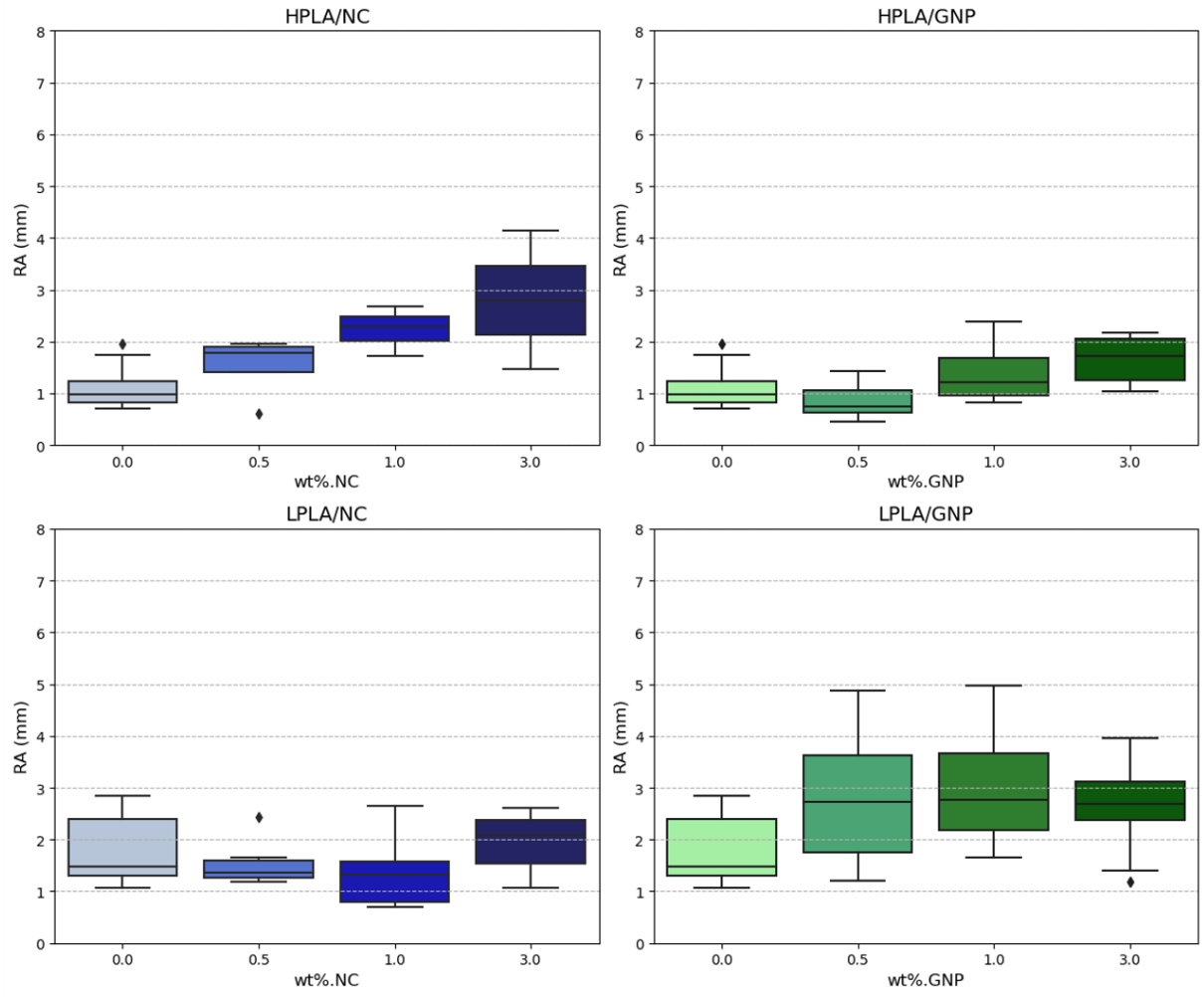

Figure 8: Roughness average (RA) of the nanocomposites with respect to composition.

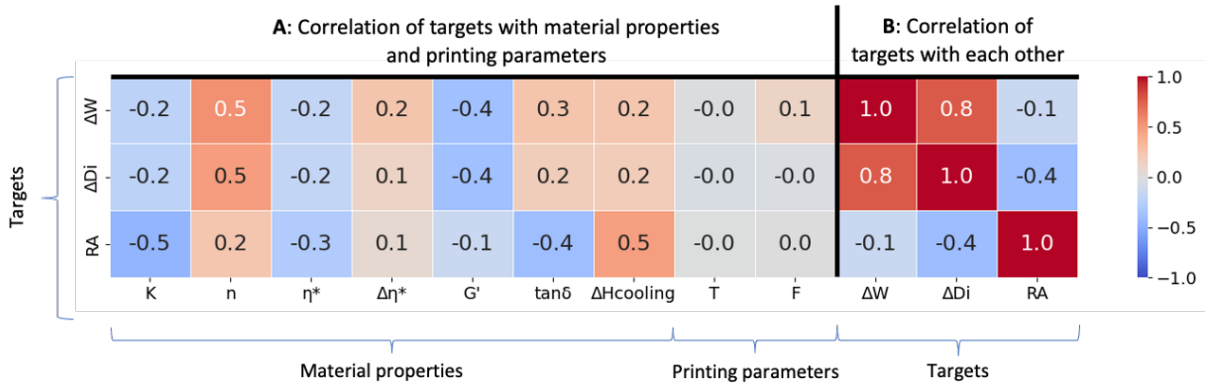

Figure 9: Pearson correlation between the material's properties, printing parameters, and printing quality.

3.2.3. Effect of material properties, and printing parameters on the printability

The previous sections focused on the effect of material viscosity and thermal degradation on ΔW, ΔD_i, and RA and competing factors were discovered. On the other hand, thermal properties such as transition temperatures or material crystallinity, other rheological properties, and printing parameters could all have an impact on printing quality, and their relationships should be investigated. The Pearson correlation coefficent describes the linear correlation between two factors. Using the dataset described in section 2.6, the Pearson correlation coefficient matrix was generated. Figure 9 displays the corresponding results as a heatmap, with each cell displaying the coefficient of correlation between two cell components. The scale of the heatmap ranges from 1 to -1, with 1 indicating direct association between two parameters, -1 indicating direct negative correlation, and 0 indicating no correlation. The correlation coefficient between targets and material properties found to be significantly low, indicating no positive or negative linear correlation between two factors. Moreover, the correlation coefficient between targets and printing parameters also found to be almost zero. On the other hand, correlation coefficient between ΔD_i and ΔW found to be around 0.8 which indicates a strong positive correlation. This result is also consistent with the previous discussions where the ΔD_i shown to have similar trend with ΔW. Between RA - ΔW, and RA - ΔD_i no direct correlation found at all. This is also consistent with the previously discussed relation between RA and ΔW where both over and under-extrusion could increase the roughness average. It is noteworthy to men-

tion that while the Pearson Correlation Coefficient found to be successful to reveal the correlation of targets with each other, it is not possible to deduce the effect of material properties or printing parameters on the targets. It is evident that these factors do not act in isolation when influencing the printing and final quality and that is why there is no single direct correlation between one target and one property. In fact, there is a complex interplay or collaboration among multiple factors at play. Given the substantial amount of experimental data and the intricate interplay between these parameters, it becomes challenging to assess the relationship between individual factors and properties.

3.3. Predicting the printing quality

For examining complex, possibly non-linear associations between features that affect the printing and final quality, machine learning algorithms like Random Forest are capable of capturing synergistic effects among various features [33, 34]. Accordingly, a Random Forest model was built to predict the ΔW using the complete dataframe where the extrusion of the failed prints were included as $\Delta W = -1.0$. Figure 10a shows the graphical assessment of predictive model for ΔW. The performance metrics of the ΔW model presented in Table 6 demonstrates strong predictive skills, as evidenced by its high R^2_{train} values of 0.87 and 0.82 for R^2_{test} respectively. The results demonstrate that the model effectively captures underlying patterns, as evidenced by the comparatively low MAE values of 0.16 for the test set and 0.12 for the training set. The feature importance analysis presented in Figure 10b indicates that the flow index, n, exhibits the highest level of impact, accounting for approximately 33% of the model's predictive capacity. The flow consistency index, K, has the second significant impact on the predictive performance of the model, accounting for approximately 19% of the significance. This suggests that these two properties have a substantial impact on the ΔW. It is noteworthy to mention that printing parameters almost have very little effect on the predictive capacity and accordingly on the ΔW.

The geometrical features of samples with $-1.0 \leq \Delta W < -0.8$ were impossible to analyse. Accordingly, another ΔW model, namely Filtered ΔW, was built by excluding the $-1.0 \leq \Delta W < -0.8$ range. The graphical assessment of the predictive model is shown

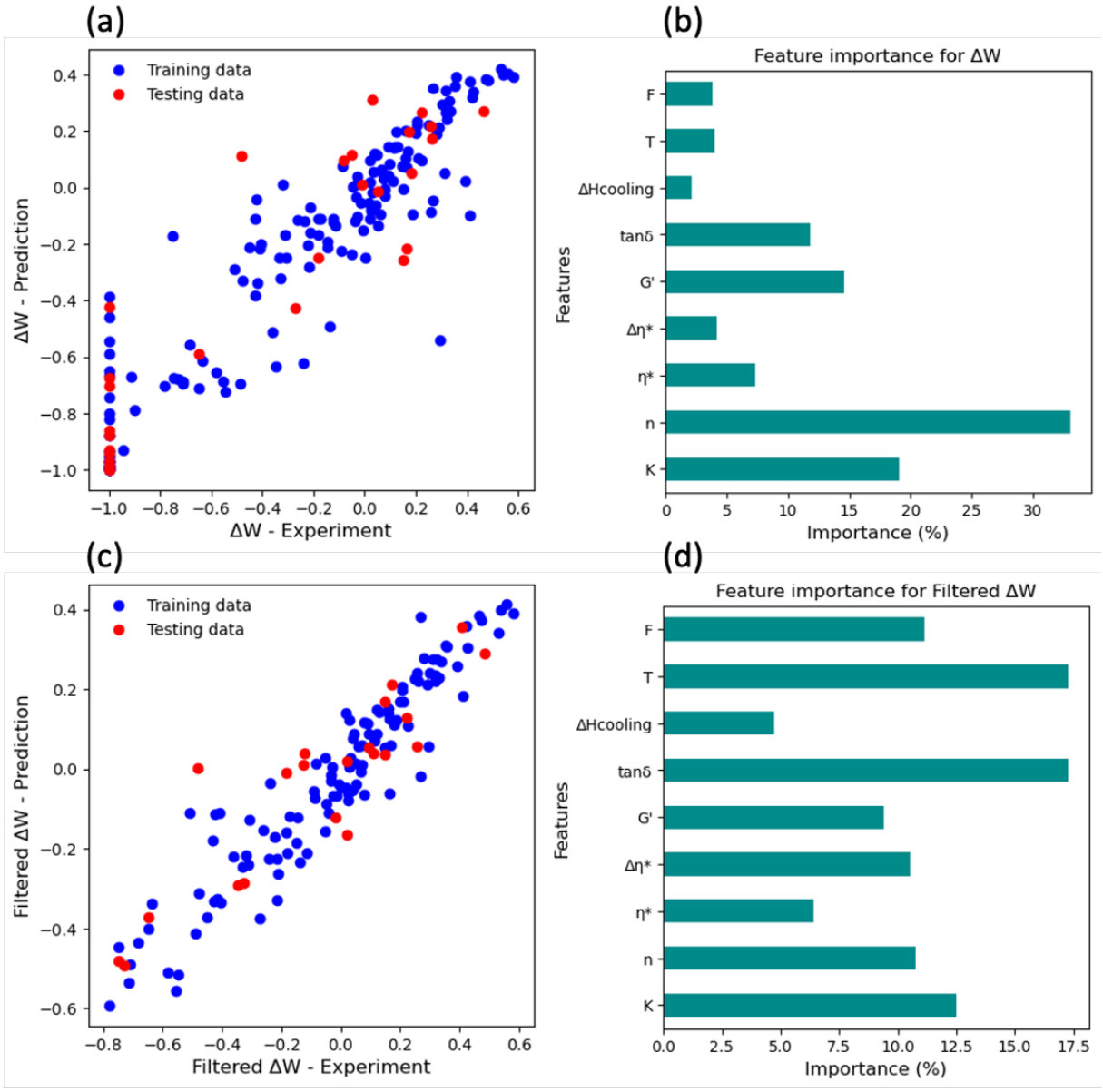

Figure 10: Graphical assessment of predictive models and feature importance analysis for ΔW. (a) Predictive model and (b) feature importance analysis of model including all ΔW, (c) predictive model and (d) feature importance analysis of model excluding the range $-1.0 \leq \Delta W < -0.8$.

in Figure 10c. The Filtered ΔW model exhibits lower R^2_{test} value of 0.73 in comparison to the initial model. However, it still exhibits a strong performance with R^2_{train} value of 0.85 with a notably low MAE (0.09) for the training set. This indicates that the model effectively captures the underlying patterns and it still exhibits robust prediction abilities, particularly demonstrated by its capacity to generalize effectively to unfamiliar data. Furthermore, the examination of feature importance (Fig.10d) exhibited a considerable shift following the exclusion of failed printings. The variable rheological loss factor, $tan\delta$, and printing parameter temperature, T, emerged as the most influential elements on the objective both having 17% of importance. The flow consistency index and the extrusion flow were the second and third most influential parameters on the predictive model.

In the first model, failed printings were included in the dataframe, and n was the most relevant variable for predicting ΔW. In the second model, $tan\delta$ and printing temperature became more prominent. The inherent nature of the flow index, which characterizes the behavior of the steady flow curve and likely exerts a greater influence on the outcome of unsuccessful printing attempts, explains this finding. The $tan\delta$ characterizes the material's viscoelastic behavior and is the ratio of storage modulus to loss modulus. Along with the printing temperature, it turned out to be more effective in predicting successful printings. The importance of forecasting successful printings (filtered ΔW) highlights the impact of viscoelastic behavior on printing stability. Also, Pearson correlation coefficients did not show any direct links between ΔW and printing parameters. However, the random forest model did show that printing parameters and material properties had a big impact on the quality of the predictions.

The geometrical features, ΔD_i and RA, of the printed samples with $\Delta W \geq -0.8$ were also predicted using Random Forest algorithm. Figure 11a. highlights the graphical assessment of the predictive model for the ΔD_i and Figure 11b. show the significance analysis of the features for predicting the ΔD_i. The model exhibits remarkable predictive capability, with a R^2_{test} value of 0.76 and a R^2_{training} value of 0.90. The MAE values for both the test and training sets are remarkably low, measuring at 0.02 and 0.01, respectively, indicating the strong accuracy of the predictions. The flow consistency coefficient was

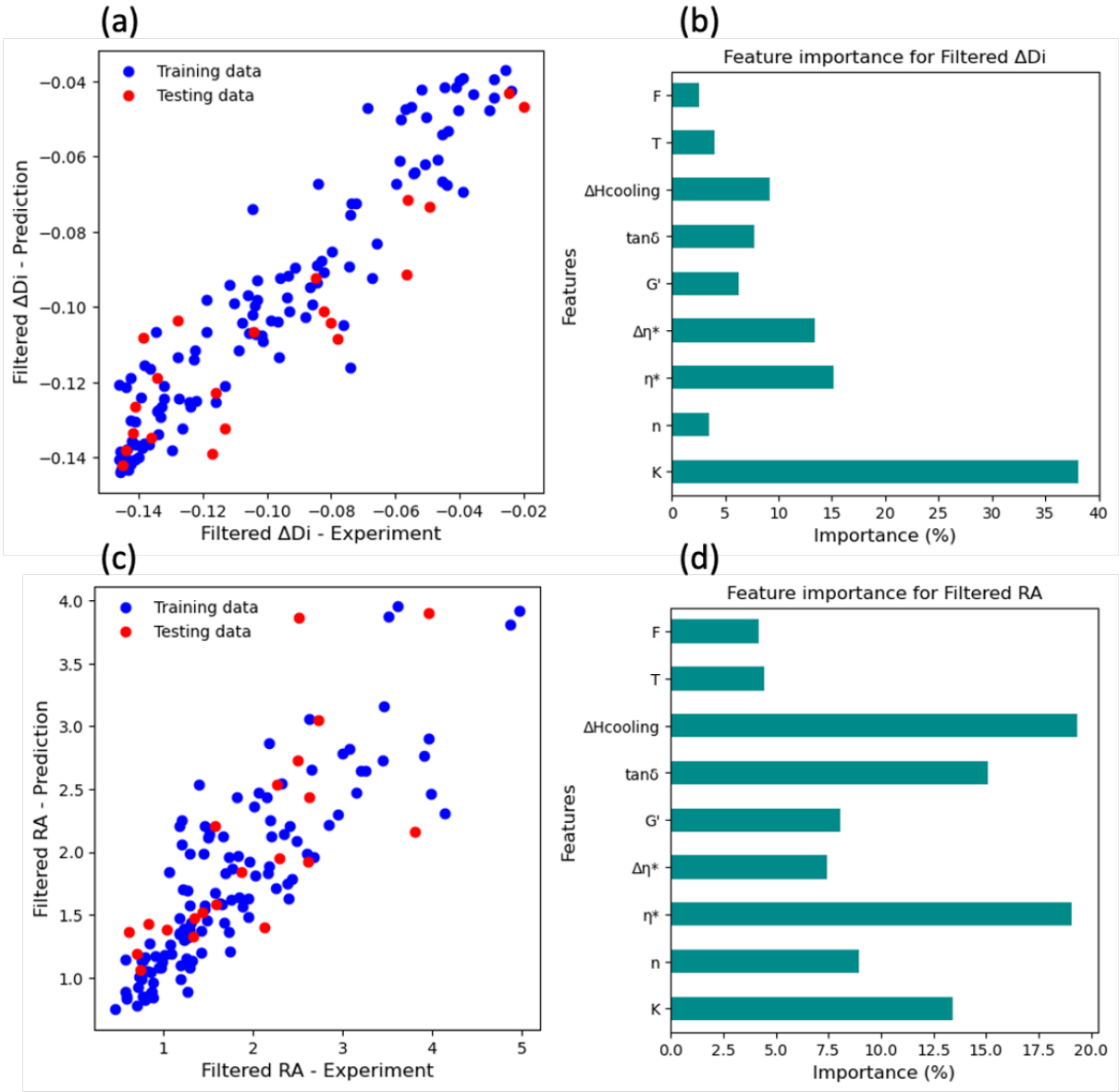

Figure 11: Graphical assessment of RF models and feature importance analysis for geometrical features. (a) Predictive model and (b) feature importance analysis of ΔD_i, (c) predictive model and (d) feature importance analysis of RA.

found to be the most influential parameter for the prediction, with an importance of 38%. The complex viscosity,η^*, and change in the complex viscosity,$\Delta\eta^*$, followed the K with significance of 15 and 13%, respectively. These findings underscore the pivotal role of material viscosity and thermal stability in shaping geometric features during the printing process.

Figure 11c presents the graphical assessment of the predictive model for RA, while Figure 11d showcases the significance analysis. Although the model targeting RA captures some variance in the data with a test R^2_{test} score of 0.57 and a training R^2_{train} score of 0.73, it falls short compared to other models assessed in this study. Furthermore, both the training and test sets exhibit rather large MAE, indicating significant differences between predicted and actual RA values. The analysis identifies several influential factors in determining RA values, with complex viscosity, flow index, and cooling enthalpy emerging as the most important. These findings align with recognized rheological principles, highlighting the crucial role of material viscosity, flow behavior, and thermal properties in shaping surface roughness during printing processes. While the model considers some of the key rheological and thermal properties, it might miss out on other important factors affecting RA. To improve the model's accuracy, a wider range of elements needs to be considered.

Table 6: Performance metrics of the predictive models.

Target	R^2_{test}	MAE_{test}	R^2_{train}	$\text{MAE}_{\text{train}}$
ΔW	0.82	0.16	0.87	0.12
Filtered ΔW	0.73	0.14	0.85	0.09
Filtered ΔD_i	0.76	0.02	0.90	0.01
Filtered RA (mm)	0.57	0.44	0.73	0.37

4. Conclusion

This study aims at quantifying the possibility and quality of 3D printing of thermoplastic-based nanocomposites. Specifically, we developed predictive models capable of determining the printability of polymer nanocomposites by employing machine learning algorithms, specifically the Random Forest algorithm. Our investigation encompassed a compre-

hensive exploration of the complex interplay between material properties and printing parameters, shedding light on the factors influencing the final printed product. The results demonstrate the efficacy of our predictive models in capturing intricate relationships between material attributes and printing outcomes such as over-/under-extrusion or variation in diameter of a cylindrical specimen. The resulting models for ΔW and ΔD_i have high R^2 values and low MAE values. Our analysis highlights the importance of considering both material properties and printing parameters when predicting printing quality. The interaction of these components highlights the intricate nature of 3D printing processes and the need for advanced modeling methods. However, challenges remain, particularly in predicting roughness average. The observed discrepancies between predicted and actual values for these parameters point towards further research on different factors that could be influential on the roughness average. Finally, our study optimizes 3D printing procedures for thermoplastic-based nanocomposites by using a predictive model to decrease trial-and-error iterations. By providing a comprehensive predictive modeling framework, this study paves the way for the adaptation of innovative materials to additive manufacturing.

Acknowledgements

We acknowledge the support from the MAD2D-CM project on Two-dimensional disruptive materials funded by the Community of Madrid, the Recovery, Transformation and Resilience Plan, and NextGenerationEU from the European Union. Additionally, M.G. was supported by the National Science Foundation Division of Material Research (Grant No. DMR2153316) through the International Research Experience for Students (IRES) program.

References

[1] W. He, P. Song, B. Yu, Z. Fang, H. Wang, Flame retardant polymeric nanocomposites through the combination of nanomaterials and conventional flame retardants, Progress in Materials Science 114 (2020) 100687. doi:10.1016/j.pmatsci.2020.100687.

[2] B. Huang, P. J. Bártolo, Rheological characterization of polymer/ceramic blends for 3d printing of bone scaffolds, Polymer Testing 68 (2018) 365–378. doi:10.1016/j.polymertesting.2018.04.033.

[3] A. D. Valino, J. R. C. Dizon, A. H. Espera, Q. Chen, J. Messman, R. C. Advincula, Advances in 3d printing of thermoplastic polymer composites and nanocomposites (11 2019). doi:10.1016/j.progpolymsci.2019.101162.

[4] Y. Xu, B. Šavija, Development of strain hardening cementitious composite (shcc) reinforced with 3d printed polymeric reinforcement: Mechanical properties, Composites Part B: Engineering 174 (10 2019). doi:10.1016/j.compositesb.2019.107011.

[5] S. Wang, Y. Ma, Z. Deng, S. Zhang, J. Cai, Effects of fused deposition modeling process parameters on tensile, dynamic mechanical properties of 3d printed polylactic acid materials, Polymer Testing 86 (6 2020). doi:10.1016/j.polymertesting.2020.106483.

[6] C. Zeng, L. Liu, W. Bian, Y. Liu, J. Leng, 4d printed electro-induced continuous carbon fiber reinforced shape memory polymer composites with excellent bending resistance, Composites Part B: Engineering 194 (8 2020). doi:10.1016/j.compositesb.2020.108034.

[7] R. Kotsilkova, S. Tabakova, R. Ivanova, Effect of graphene nanoplatelets and multi-walled carbon nanotubes on the viscous and viscoelastic properties and printability of polylactide nanocomposites, Mechanics of Time-Dependent Materials 26 (2022) 611–632. doi:10.1007/s11043-021-09503-2.

[8] R. Kotsilkova, S. Tabakova, Exploring effects of graphene and carbon nanotubes on rheology and flow instability for designing printable polymer nanocomposites, Nanomaterials 13 (3 2023). doi:10.3390/nano13050835.

[9] M. Bertolino, D. Battegazzore, R. Arrigo, A. Frache, Designing 3d printable polypropylene: Material and process optimisation through rheology, Additive Manufacturing 40 (4 2021). doi:10.1016/j.addma.2021.101944.

[10] R. Ivanova, R. Kotsilkova, Rheological study of poly(lactic) acid nanocomposites with carbon nanotubes and graphene additives as a tool for materials characterization for 3d printing application, Applied Rheology 28 (2018). doi:10.3933/ApplRheol-28-54014.

[11] M. V. Candal, I. Calafel, N. Aranburu, M. Fernández, G. Gerrica-Echevarria, A. Santamaría, A. J. Müller, Thermo-rheological effects on successful 3d printing of biodegradable polyesters, Additive Manufacturing 36 (12 2020). doi:10.1016/j.addma.2020.101408.

[12] Y. Zhang, S. K. Moon, Data-driven design strategy in fused filament fabrication: Status and opportunities (4 2021). doi:10.1093/jcde/qwaa094.

[13] J. R. Deneault, J. Chang, J. Myung, D. Hopper, A. Armstrong, M. Pitt, B. Maruyama, Toward autonomous additive manufacturing: Bayesian optimization on a 3d printer, MRS Bulletin 46 (2021).

[14] Z. Li, Z. Zhang, J. Shi, D. Wu, Prediction of surface roughness in extrusion-based additive manufacturing with machine learning, Robotics and Computer-Integrated Manufacturing 57 (2019) 488–495. doi:10.1016/j.rcim.2019.01.004.

[15] Z. Zhang, L. Poudel, Z. Sha, W. Zhou, D. Wu, Data-driven predictive modeling of tensile behavior of parts fabricated by cooperative 3d printing, Journal of Computing and Information Science in Engineering 20 (1 2020). doi:10.1115/1.4045290.

[16] P. Sharma, H. Vaid, R. Vajpeyi, P. Shubham, K. M. Agarwal, D. Bhatia, Predicting the dimensional variation of geometries produced through fdm 3d printing employing supervised machine learning, Sensors International 3 (1 2022). doi:10.1016/j.sintl.2022.100194.

[17] Y. Ma, M. A. Schutyser, R. M. Boom, L. Zhang, Predicting the extrudability of complex food materials during 3d printing based on image analysis and gray-box data-driven modelling, Innovative Food Science and Emerging Technologies 73 (10 2021). doi:10.1016/j.ifset.2021.102764.

[18] H. Nakajima, M. Takahashi, Y. Kimura, Induced crystallization of plla in the presence of 1, 3, 5-benzenetricarboxylamide derivatives as nucleators: Preparation of haze-free crystalline plla materials, Macromolecular Materials and Engineering 295 (5) (2010) 460–468. doi:doi.org/10.1002/mame.200900353.

[19] Q. Fang, M. A. Hanna, Rheological properties of amorphous and semicrystalline polylactic acid polymers, Industrial Crops and Products 10 (1) (1999) 47–53. doi:https://doi.org/10.1016/S0926-6690(99)00009-6.

[20] M. Hernández-del Valle, C. Schenk, L. Echevarría-Pastrana, B. Ozdemir, E. Dios-Lázaro, J. Ilarraza-Zuazo, D.-Y. Wang, M. Haranczyk, Robotically automated 3d printing and testing of thermoplastic material specimens, Digital Discovery 2 (6) (2023) 1969–1979. doi:10.1039/D3DD00141E.

[21] D. Whitehouse, Surfaces and their Measurement, 1st Edition, Elsevier, 2012.

[22] L. Breiman, Random forests, Machine learning 45 (2001) 5–32. doi:10.1023/A:1010933404324.

[23] F. Pedregosa, G. Varoquaux, A. Gramfort, V. Michel, B. Thirion, O. Grisel, M. Blondel, P. Prettenhofer, R. Weiss, V. Dubourg, J. Vanderplas, A. Passos, D. Cournapeau, M. Brucher, M. Perrot, E. Duchesnay, Scikit-learn: Machine learning in Python, Journal of Machine Learning Research 12 (2011) 2825–2830.

[24] D. Sun, H. Wen, D. Wang, J. Xu, A random forest model of landslide susceptibility mapping based on hyperparameter optimization using bayes algorithm, Geomorphology 362 (2020) 107201. doi:10.1016/j.geomorph.2020.107201.

[25] B. Sumathi, et al., Grid search tuning of hyperparameters in random forest classifier for customer feedback sentiment prediction, International Journal of Advanced Computer Science and Applications 11 (9) (2020). doi:10.14569/ijacsa.2020.0110920.

[26] N. Najafi, M. C. Heuzey, P. J. Carreau, P. M. Wood-Adams, Control of thermal degradation of polylactide (pla)-clay nanocomposites using chain extenders, Polymer Degradation and Stability 97 (2012) 554–565. doi:10.1016/j.polymdegradstab.2012.01.016.

[27] Q. Meng, M. C. Heuzey, P. J. Carreau, Control of thermal degradation of polylactide/clay nanocomposites during melt processing by chain extension reaction, Polymer Degradation and Stability 97 (2012) 2010–2020. doi:10.1016/j.polymdegradstab.2012.01.030.

[28] A. A. Cuadri, J. E. Martín-Alfonso, Thermal, thermo-oxidative and thermomechanical degradation of pla: A comparative study based on rheological, chemical and thermal properties, Polymer Degradation and Stability 150 (2018) 37–45. doi:10.1016/j.polymdegradstab.2018.02.011.

[29] A. K. Mohanty, M. Misra, L. T. Drzal, Natural fibers, biopolymers, and biocomposites, CRC press, 2005.

[30] F. d Kopinke, M. Remmler, K. Mackenzie, M. Milder, Thermal decomposition of biodegradable polyesters-11. poly(lactic acid) (1996).

[31] S. Kashi, R. K. Gupta, N. Kao, S. A. Hadigheh, S. N. Bhattacharya, Influence of graphene nanoplatelet incorporation and dispersion state on thermal, mechanical and electrical properties of biodegradable matrices, Journal of Materials Science and Technology 34 (2018) 1026–1034. doi:10.1016/j.jmst.2017.10.013.

[32] P. Manafi, I. Ghasemi, M. Karrabi, H. Azizi, M. R. Manafi, P. Ehsaninamin, Thermal stability and thermal degradation kinetics (model-free kinetics) of nanocomposites based on poly (lactic acid)/graphene: the influence of functionalization, Polymer Bulletin 72 (2015) 1095–1112. doi:10.1007/s00289-015-1325-4.

[33] A. Cutler, D. R. Cutler, J. R. Stevens, Random forests, Ensemble machine learning: Methods and applications (2012) 157–175.

[34] J.-W. Su, D. Li, Y. Xie, T. Zhou, W. Gao, H. Deng, M. Xin, J. Lin, A machine learning workflow for 4d printing: understand and predict morphing behaviors of printed active structures, Smart Materials and Structures 30 (1) (2020) 015028.